

# Studies of the distinct regions due to CO selective dissociation in the Aquila molecular cloud

Toktarkhan Komesh<sup>1,2,3</sup>, Willem Baan<sup>1,4</sup>, Jarken Esimbek<sup>1,5</sup>, Jianjun Zhou<sup>1,5</sup>, Dalei Li<sup>1,5</sup>, Gang Wu<sup>1,5</sup>, Yuxin He<sup>1,5</sup>, Zulfazli Rosli<sup>6</sup>, and Margulan Ibraimov<sup>3</sup>

<sup>1</sup> Xinjiang Astronomical Observatory, Chinese Academy of Sciences, Urumqi 830011, PR China  
e-mail: komesh.t@outlook.com, baan@astron.nl, jarken@xao.ac.cn

<sup>2</sup> University of the Chinese Academy of Sciences, Beijing 100080, PR China

<sup>3</sup> Department of Solid State Physics and Nonlinear Physics, Faculty of Physics and Technology, Al-Farabi Kazakh National University, Almaty, 050040, Kazakhstan

<sup>4</sup> Netherlands Institute for Radio Astronomy, ASTRON, 7991 PD, Dwingeloo, The Netherlands

<sup>5</sup> Key Laboratory of Radio Astronomy, Chinese Academy of Sciences, Urumqi 830011, PR China

<sup>6</sup> The Department of Physics, Faculty of Science, University of Malaya, 50603, Kuala Lumpur, Malaysia

Submitted to A&A

Accepted 26 Oct 2020

## ABSTRACT

**Aims.** We investigate the role of selective dissociation in the process of star formation by comparing the physical parameters of protostellar-prestellar cores and the distinct regions with the CO isotope distributions in photo-dissociation regions. We seek to understand whether there is a better connection between the evolutionary age of star forming regions and the effect of selective dissociation

**Methods.** Wide-field observations of the  $^{12}\text{CO}$ ,  $^{13}\text{CO}$ , and  $\text{C}^{18}\text{O}$  ( $J=1-0$ ) emission lines are used to study the ongoing star formation activity in the Aquila molecular region, and the  $70\mu\text{m}$  and  $250\mu\text{m}$  data are used to describe the heating of the surrounding material and as an indicator of the evolutionary age of the core.

**Results.** The protostellar-prestellar cores are found at locations with the highest  $\text{C}^{18}\text{O}$  column densities and their increasing evolutionary age would relate to an increasing  $70\mu\text{m}/250\mu\text{m}$  emission ratio at their location. An evolutionary age of the cores may also follow from the  $^{13}\text{CO}$  versus  $\text{C}^{18}\text{O}$  abundance ratio, which decreases with increasing  $\text{C}^{18}\text{O}$  column densities. The original mass has been estimated for nine representative star formation regions and the original mass of the region correlated well with the integrated  $70\mu\text{m}$  flux density. Similarly, the  $X_{^{13}\text{CO}}/X_{\text{C}^{18}\text{O}}$  implying the dissociation rate for these regions correlates with the  $70\mu\text{m}/250\mu\text{m}$  flux density ratio and reflects the evolutionary age of the star formation activity.

**Key words.** ISM: clouds — evolution — ISM: abundances — ISM: molecules — photon-dominated region (PDR) — stars: formation

## 1. Introduction

The Aquila rift is part of a dark lane of cosmic dust flowing prominently through the central region of the galactic plane of the Milky Way, forming the Great Rift. The two known sites of star formation in the Aquila Rift cloud complex – the Serpens South (Bontemps et al. 2010) and the W40 HII region (Smith et al. 1985) become a hot spot for the study of star formation. Spitzer observations show that W40, and the embedded cluster Serpens South nearby on the sky such that the Serpens South is seemingly part of the more evolved W40 region (Gutermuth et al. 2008). The distance to Serpens Main and W40 has recently measured to be 436 pc, and the distance to Serpens South should be similar because the two sources are kinematically connected (Ortiz-León et al. 2017). Su et al. (2020) estimated the mass  $\sim 1.4 \times 10^5 M_{\odot}$  for the W40 giant molecular cloud determining the distance  $\sim 474$  pc.

Recently, Könyves et al. (2015) presented the results of the Herschel Gould Belt survey (HGBS) observations in the Aquila molecular cloud complex, imaged with the SPIRE and PACS photometric cameras from  $70\mu\text{m}$  to  $500\mu\text{m}$ . They identified a complete sample of starless dense cores and embedded (Class 0-I) protostars in the Aquila molecular cloud complex using the

multi-scale, multi-wavelength source extraction algorithm. In this study, we use the  $70\mu\text{m}$  and  $250\mu\text{m}$  data to describe the heating of the surrounding material and as an indicator of the evolutionary age of the core.

In this work, we encounter regions that are called photo-dissociation regions (PDRs) and we encounter regions where we suspect that also selective dissociation plays a role. We investigate the role of selective dissociation in the process of star formation by comparing the physical parameters of protostellar-prestellar cores and the distinct regions with the CO isotope distributions in photo-dissociation regions. We seek to understand whether there is a better connection between the evolutionary age of star forming regions and the effect of selective dissociation. But the detailed description of how selective dissociation works should be moved to Section 3.6. As star formation process progresses, the far-ultraviolet photons will start to regulate both the heating and the chemistry of the resulting PDR (Tielens, & Hollenbach 1985). As a result of the UV radiation field, selective dissociation of CO is an expected phenomenon in PDRs (Glassgold et al. 1985; Yurimoto & Kuramoto 2004). In this process, UV radiation selectively dissociates less-abundant CO isotopologues more

effectively than more-abundant ones, owing to different levels of self-shielding (van Dishoeck & Black 1988; Liszt 2007; Shimajiri et al. 2014). Since several regions have been identified as distinct star formation regions in the H<sub>2</sub>CO absorption map of the Aquila MC (Komesh et al. 2019), a comparison is made between the C<sup>18</sup>O distribution and the H<sub>2</sub>CO absorption.

In the present paper, we show the results of the <sup>12</sup>CO, <sup>13</sup>CO and C<sup>18</sup>O observations toward the W40 and Serpens South regions of Aquila Rift. In Section 2, we present the details of the observations. The results and discussions are described in Section 3. Finally, the conclusions are in Section 4.

## 2. Archival data

The <sup>12</sup>CO(1 – 0), <sup>13</sup>CO(1 – 0) and C<sup>18</sup>O(1 – 0) data, simultaneously observed using the 13.7 m millimeter wave telescope of the Purple Mountain Observatory in Delingha, have been taken from the Millimeter Wave Radio Astronomy Database<sup>1</sup>. The central position of the on-the-fly observing pattern is 18<sup>h</sup>30<sup>m</sup>03<sup>s</sup> –2°02′40″(J2000). The half-power beamwidth (HPBW) of the observing system is ~ 50 ″, the velocity resolution is 0.17 km s<sup>-1</sup> and the system temperature ranged from 180 to 320 K. The <sup>12</sup>CO(1 – 0), <sup>13</sup>CO(1 – 0) and C<sup>18</sup>O(1 – 0) data have been smoothed to the same spatial resolution of 60 ″ and cell size is 30 ″. The one sigma noise levels of the <sup>12</sup>CO, <sup>13</sup>CO and C<sup>18</sup>O data are 0.5 K, 0.35 K, and 0.35 K, respectively. Assuming a distance of 436 pc for the Aquila complex, the spatial scale of the maps is 0.124 pc arcmin<sup>-1</sup>.

The infrared 70 μm and 250 μm images (André et al. 2010) were obtained from The Herschel Gould Belt Survey Archive<sup>2</sup>.

## 3. Results and discussion

### 3.1. <sup>12</sup>CO(1 – 0) Emission Line

The integrated intensity map of <sup>12</sup>CO(1-0) over a velocity range 2 < V<sub>LSR</sub> < 12 km s<sup>-1</sup> with signal-to-noise ratio greater than three is presented in Figure 1a. Enhanced core emission is present around W40 on the north and west sides that could result from heating by the H II region. There is weak emissions around Serpens South. The brightest position is at (RA,Dec) = (18<sup>h</sup>31<sup>m</sup>15<sup>s</sup>, –2°08′13″).

### 3.2. <sup>13</sup>CO(1 – 0) Emission Line

The integrated intensity map of <sup>13</sup>CO(1–0) over a velocity range 2 < V<sub>LSR</sub> < 12 km s<sup>-1</sup> and a signal-to-noise ratio greater than three is presented in Figure 1b. Here also, enhanced emission is seen on the north and west side of W40. There are several elongated structures at Serpens South.

### 3.3. C<sup>18</sup>O(1 – 0) Emission Line

The integrated intensity map of C<sup>18</sup>O(1–0) over a velocity range 2 < V<sub>LSR</sub> < 12 km s<sup>-1</sup> is presented in Figure 1c with its signal-to-noise ratio greater than three. Several integrated intensity concentrations are present in this map including both the W40 H II region and Serpens South. The distribution of the C<sup>18</sup>O(1 – 0) emission has some similarity to the Herschel 250 μm large scale (~0.124 pc) image presented in Figure 1d. Both the C<sup>18</sup>O and the Herschel data trace the same regions, which suggests that

the C<sup>18</sup>O and the Herschel 250 μm emission arise from similar regions.

### 3.4. Column densities and abundance Ratios

The excitation temperature,  $T_{\text{ex}}$ , was estimated from the peak brightness temperature of <sup>12</sup>CO(1 – 0), by the following equation with the assumption that the <sup>12</sup>CO(1 – 0) is optically thick and the beam-filling factor of one (e.g., Pineda et al. 2010; Kong et al. 2015; Lin et al. 2016):

$$T_{\text{ex}} = \frac{hv_{12\text{CO}}}{k} \left[ \ln \left( 1 + \frac{hv_{12\text{CO}}/k}{T_{\text{mb},12\text{CO}} + J_v(T_{\text{bg}})} \right) \right]^{-1} \text{K}$$

$$= 5.53 \left[ \ln \left( 1 + \frac{5.53}{T_{\text{mb},12\text{CO}} + 0.818} \right) \right]^{-1} \text{K}, \quad (1)$$

where  $T_{\text{mb},12\text{CO}}$  is the peak intensity of <sup>12</sup>CO(1 – 0) in units of K,  $J_v(T) = \frac{hv/k}{\exp(hv/kT) - 1}$  is the effective radiation temperature (Ulich & Haas 1976), and  $T_{\text{bg}} = 2.7$  K is the temperature of cosmic microwave background radiation. The estimated excitation temperatures in the whole observed region ranges from 3.6 to 23.6 K, but these values are underestimates in locations where the <sup>12</sup>CO emission affected by the self-absorption. We assume that the excitation temperatures ( $T_{\text{ex}}$ ) of <sup>13</sup>CO and C<sup>18</sup>O lines have the same value as that of the optically thick <sup>12</sup>CO line. The optical depth and the column densities of <sup>13</sup>CO(1 – 0) and C<sup>18</sup>O(1 – 0) were estimated using the following equations on the assumption that the cloud is in LTE (e.g., Lada et al. 1994; Kawamura et al. 1998; Lin et al. 2016):

$$\tau(\text{C}^{18}\text{O}) = -\ln \left[ 1 - \frac{T_{\text{mb},\text{C}^{18}\text{O}}}{5.27[J_1(T_{\text{ex}}) - 0.166]} \right], \quad (2)$$

$$\tau(\text{C}^{13}\text{CO}) = -\ln \left[ 1 - \frac{T_{\text{mb},\text{C}^{13}\text{CO}}}{5.29[J_2(T_{\text{ex}}) - 0.164]} \right] \quad (3)$$

and

$$N(\text{C}^{18}\text{O}) = 2.42 \times 10^{14} \frac{\tau(\text{C}^{18}\text{O})\Delta V(\text{C}^{18}\text{O})T_{\text{ex}}}{1 - \exp(-5.27/T_{\text{ex}})} \quad (4)$$

$$N(\text{C}^{13}\text{CO}) = 2.42 \times 10^{14} \frac{\tau(\text{C}^{13}\text{CO})\Delta V(\text{C}^{13}\text{CO})T_{\text{ex}}}{1 - \exp(-5.29/T_{\text{ex}})} \quad (5)$$

where  $J_1(T_{\text{ex}}) = 1/[\exp(5.27/T_{\text{ex}}) - 1]$ , and  $J_2(T_{\text{ex}}) = 1/[\exp(5.29/T_{\text{ex}}) - 1]$ ,  $\Delta V$  is the FWHMs in km s<sup>-1</sup>. The abundance ratio,  $X(\text{C}^{13}\text{CO})/X(\text{C}^{18}\text{O})$ , is equivalent to the  $N(\text{C}^{13}\text{CO})/N(\text{C}^{18}\text{O})$  column density ratio.

In the regions where the <sup>12</sup>CO emission affected by the self-absorption the column densities of <sup>13</sup>CO and C<sup>18</sup>O are affected by underestimates of  $T_{\text{ex}}$  from the <sup>12</sup>CO data. This gives underestimates for the column densities of <sup>13</sup>CO and C<sup>18</sup>O in those areas. The resulting ranges of  $N(\text{C}^{13}\text{CO})$  and  $N(\text{C}^{18}\text{O})$  are  $3.8 \times 10^{14} - 5.5 \times 10^{16}$  cm<sup>-2</sup> and  $2 \times 10^{14} - 3.4 \times 10^{15}$ , respectively. And the resulting ranges of the abundance ratio of R<sub>13/18</sub> is 1.02–41.9. A map of the column density of C<sup>18</sup>O(1 – 0) is represented in Figure 2. The black stars and triangles present the locations of the protostellar and prestellar cores, respectively (Könyves et al. 2015).

The column density of C<sup>18</sup>O(1 – 0) versus the number of pixels with C<sup>18</sup>O(1 – 0) is displayed in the diagrams of Figure 3 together with the observed column densities at the location of the prestellar and protostellar cores. The cores sample locations

<sup>1</sup> <http://www.radioast.nsd.cn>

<sup>2</sup> <http://www.herschel.fr>

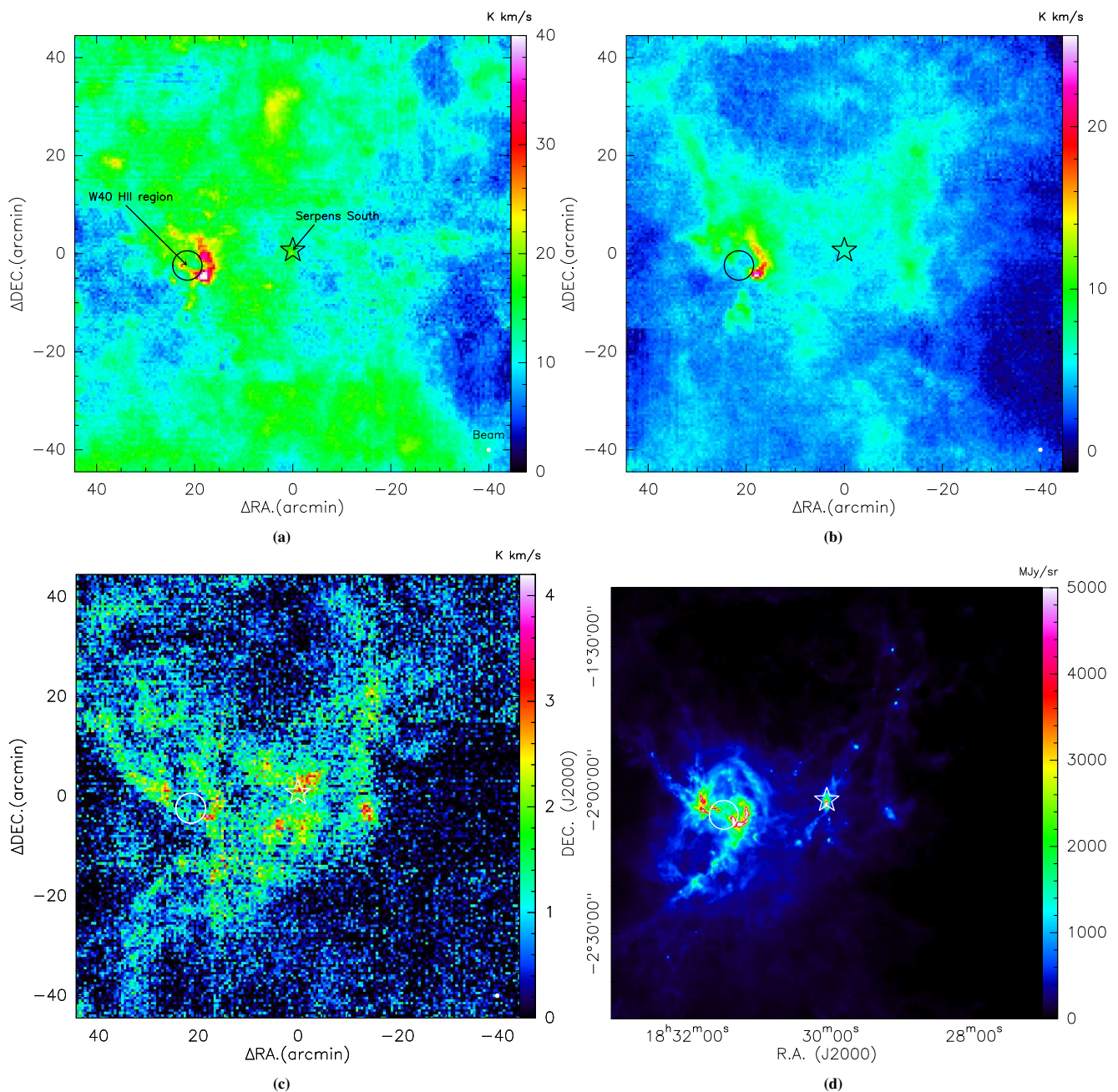


**Fig. 1.** Aquila maps of the intensities of (a)  $^{12}\text{CO}(1-0)$ , (b)  $^{13}\text{CO}(1-0)$ , (c)  $\text{C}^{18}\text{O}(1-0)$  integrated from  $2\text{ km s}^{-1}$  to  $12\text{ km s}^{-1}$ . Bottom-right white filled circles in each panel illustrate the beam size of  $60''$ . (d) The Herschel  $250\ \mu\text{m}$  image (the beam size is  $18.2''$ ) taken from André et al. (2010). The circle and star present the locations of the W40 H II region (radius  $\sim 3'$ ) and the Serpens South.

with increasing  $\text{C}^{18}\text{O}$  column densities confirming that star formation first happens in regions with the highest column densities. Most of the  $\text{C}^{18}\text{O}(1-0)$  detection points correspond to the column densities between  $0.5 \times 10^{15} \sim 1.6 \times 10^{15}\text{ cm}^{-2}$  (see panel a). The prestellar and protostellar cores correlate well with the  $\text{C}^{18}\text{O}$  column density. The majority of the prestellar cores located at the column densities between  $0.5 \times 10^{15} \sim 2 \times 10^{15}\text{ cm}^{-2}$  while the protostellar cores located at the column densities between  $0.5 \times 10^{15} \sim 2.8 \times 10^{15}\text{ cm}^{-2}$ .

### 3.5. The Far-infrared distribution

The peak flux density at the prestellar and protostellar cores at  $70\ \mu\text{m}$  and  $250\ \mu\text{m}$  are presented versus the column density

of  $\text{C}^{18}\text{O}(1-0)$  diagrams in Figure 4. The  $70\ \mu\text{m}$  diagram (panel a) shows a clear separation indicated with a dotted line between the prestellar and protostellar core distributions; most of prestellar cores have a lower flux density while most of the protostellar cores have a higher flux that may increase slightly at higher column densities. However, excepting the uncertainty of the  $N(\text{C}^{18}\text{O})$ , the  $250\ \mu\text{m}$  distribution in panel (b) shows an increasing trend with the column density suggesting that star formation is more advanced at higher column densities and that an increasing volume is affected by the ongoing star formation. The star formation processes are slower at the lower column density and requires a longer time to heat the surrounding environment. In addition, the number of protostellar (or prestellar) cores may be larger because of fragmentation which will accelerate

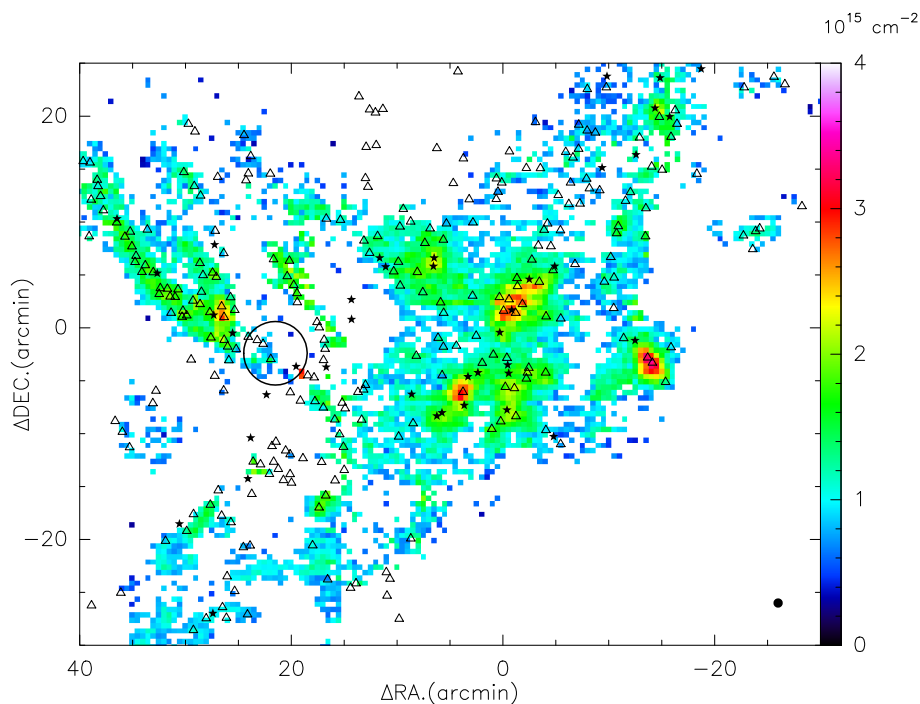


**Fig. 2.** A map of the column density of  $C^{18}O(1-0)$ . The black stars and triangles present the locations of protostellar and prestellar cores, respectively. The coordinates of the protostellar and prestellar cores were taken from Könyves et al. (2015). The black circle present the location of the W40 H II region (radius  $\sim 3'$ ) and the black filled circle in the bottom-right illustrates the beam size of  $60''$ . The clipping level for the  $^{13}CO$  and  $C^{18}O$  data was the signal-to-noise ratio greater than five. Gaussian fitting to each pixel was done.

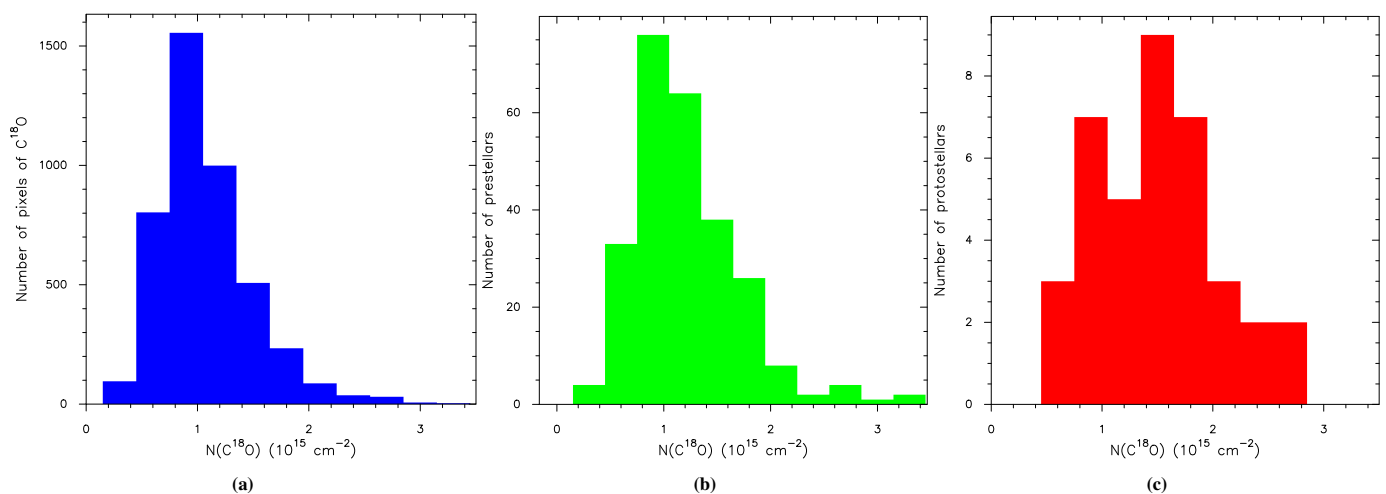


**Fig. 3.** Histograms of the distributions of (a) the number of pixels with certain column density of  $C^{18}O(1-0)$ , (b) the number of prestellar cores with this density, and (c) the protostellar cores with this column density. The prestellar and protostellar sources clearly sample the larger  $C^{18}O$  column densities.

the heating process. The number of cores with very high column density is much smaller than for low column density cores, which agrees with the histogram of the stellar core number vs. the  $C^{18}O$  column density in Figure 3.

### 3.6. Selective Photodissociation

A map of the abundance ratio  $X_{^{13}CO}/X_{C^{18}O}$  is presented in Figure 5. The contours show the value of  $X_{^{13}CO}/X_{C^{18}O}=4$ . We selected nine unique regions (A-I) in the map where the abundance ratio has a lower value (A, B, C, E, F, and G), one region with a much higher value (region D), and two regions on

the outskirts with medium values (H and I). The abundance ratio located in region D, next to the W40 H II region, is as high as 42, which is significantly larger than the 5.5 seen in the solar system (Anders & Grevesse 1989). The region D is located next to the W40 (north-west side), the region B is Serpens South and the region G was identified as distinct star formation region by Komesch et al. (2019). For the FUV emissions with sufficient energy to photo-dissociate  $^{12}CO$  it promptly becomes optically thick as it penetrates into molecular clouds. On the contrary,  $C^{18}O$  self-shielding is relatively less significant due to its low abundance and the shift of its absorption lines. Hence, this infers that the FUV emission with higher energy than the  $C^{18}O$  dissociation level will penetrate deeper into a molecular cloud

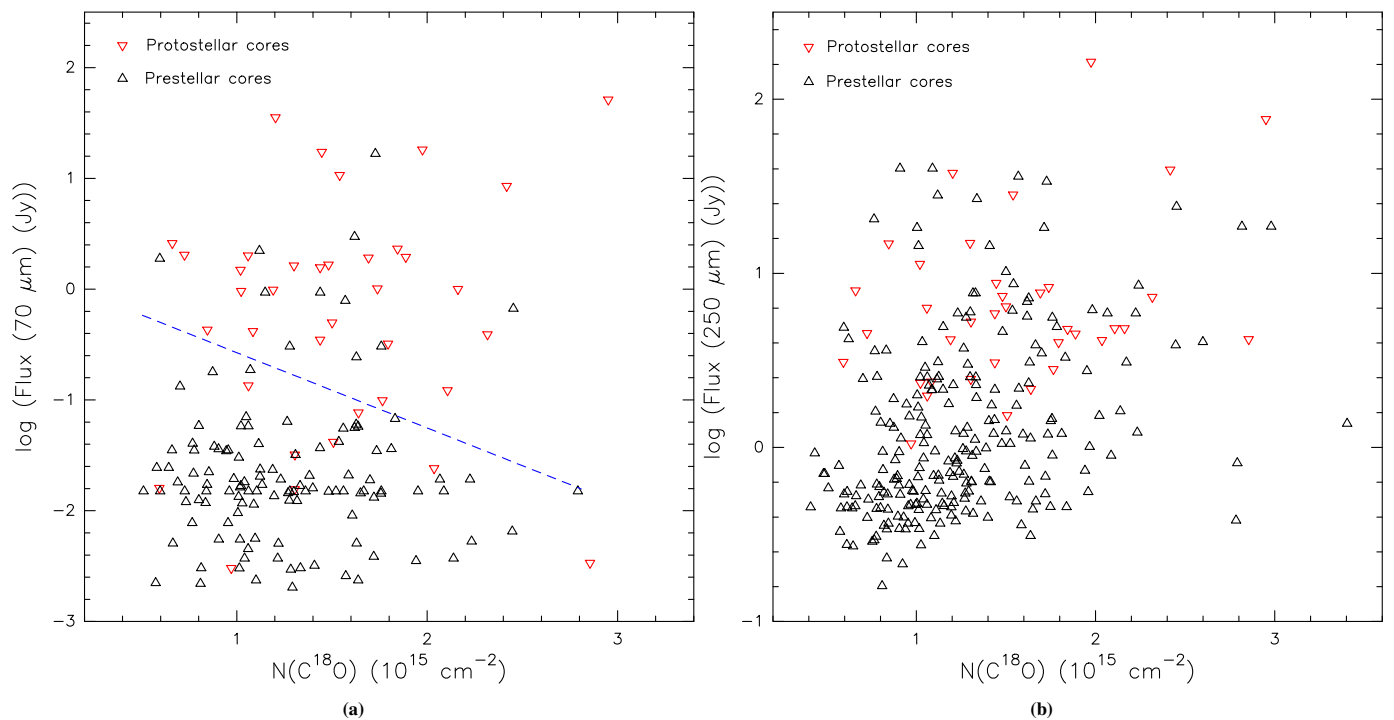


**Fig. 4.** The column density of  $C^{18}O$  vs. the peak flux densities of protostellar (red triangles) and prestellar (black triangles) cores at (a)  $70 \mu\text{m}$  and (b)  $250 \mu\text{m}$  selected from Kónyves et al. (2015). The number of prestellar cores in panel (a) is less than the total number because some have no  $70 \mu\text{m}$  flux. A clear separation is found between prestellar and protostellar cores in panel (a) (with dotted line). Panel (b) shows an increase trend of the  $250 \mu\text{m}$  flux density with the  $C^{18}O$  column density suggesting that star formation is more advanced at higher column densities and that an increasing volume is affected by the ongoing star formation.

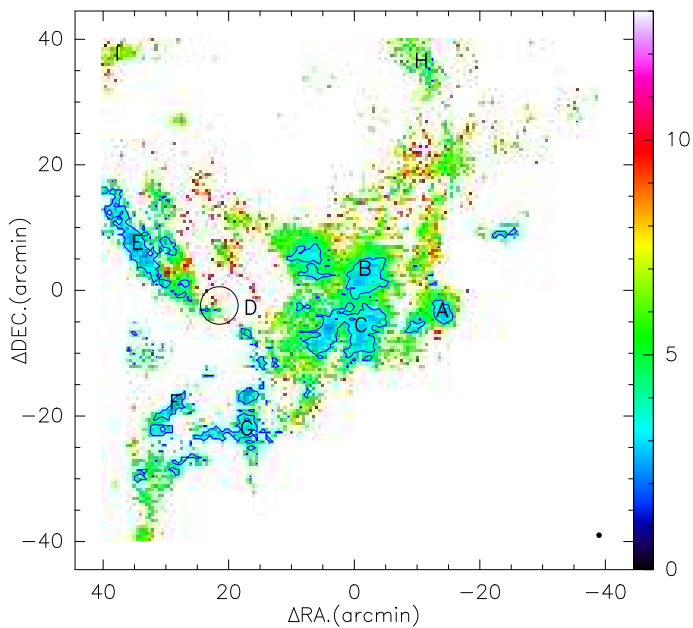


**Fig. 5.** A map of the abundance ratio  $X_{13CO}/X_{C^{18}O}$ . The contours show the value of  $X_{13CO}/X_{C^{18}O}=4$ . The letters (A-I) present the selected regions where the abundance ratio lower (A, B, C, E, F, and G) and much higher (region D), and the outskirts parts (H and I). The black circle present the location of the W40 HII region (radius  $\sim 3'$ ) and the black filled circle in the bottom-right illustrates the beam size of  $60''$ . The clipping level for the  $^{13}CO$  and  $C^{18}O$  data was the signal-to-noise ratio greater than five. High abundance ratio values are distributed only in region D and it reaches up to 42.

and also, will increase the abundance ratio of  $^{13}CO$  and  $C^{18}O$ ,  $X_{13CO}/X_{C^{18}O}$ , at the instance when  $C^{18}O$  self-shielding is not yet dominant. When both self-shielding effects of  $^{13}CO$  and  $C^{18}O$  become significant, the abundance ratio will decrease towards its intrinsic value, which is derived from the elements,  $^{12}C$ ,  $^{13}C$ ,  $^{16}O$ , and  $^{18}O$  abundances (van Dishoeck & Black 1988; Liszt 2007; Shimajiri et al. 2014). Thus, we confirm that selective FUV photodissociation of  $C^{18}O$  indeed occurs.

Figure 6 presents the averaged spectra of  $^{12}CO(1-0)$ ,  $^{13}CO(1-0)$  and  $C^{18}O(1-0)$  emissions at the nine selected regions. It is clearly seen that the central component of the broader  $^{12}CO$  are depleted by self-absorption. However, the spectrum shapes of  $^{13}CO$  and  $C^{18}O$  look different from that of  $^{12}CO$ .

### 3.7. The integrated properties of the distinct regions

The molecular hydrogen gas masses ( $M_{H_2}$ ) of the selected A-I regions has been derived using the equations in Tan et al. (2013). In order to estimate the original mass of the selected regions, the profile of the  $^{12}CO$  emission line has been fitted with Gaussian using the line wings of the self-absorbed  $^{12}CO$  lines (see Figure 7).

We compute the  $^{12}CO$  luminosity as follows:

$$L_{CO} = I_{avg} \times N_{pix} \times 23.5 \times (D \times \Delta_{pix})^2, \quad (6)$$

where  $L_{CO}$  is the  $^{12}CO$  luminosity in  $K \text{ kms}^{-1} \text{ pc}^2$ ,  $I_{avg}$  is the average  $^{12}CO$  intensity ( $K \text{ kms}^{-1}$ ) obtained from the integrated intensity map on main-beam temperature scale,  $N_{pix}$  is the number of pixels included,  $D$  is the distance to the sources in Mpc and  $\Delta_{pix}$  is the pixel size in arcseconds. The mass of the molecular gas is computed using:

$$M_{H_2} = 1.6 \times 10^{-20} \times L_{CO} \times X_{CO} \quad (M_{\odot}), \quad (7)$$

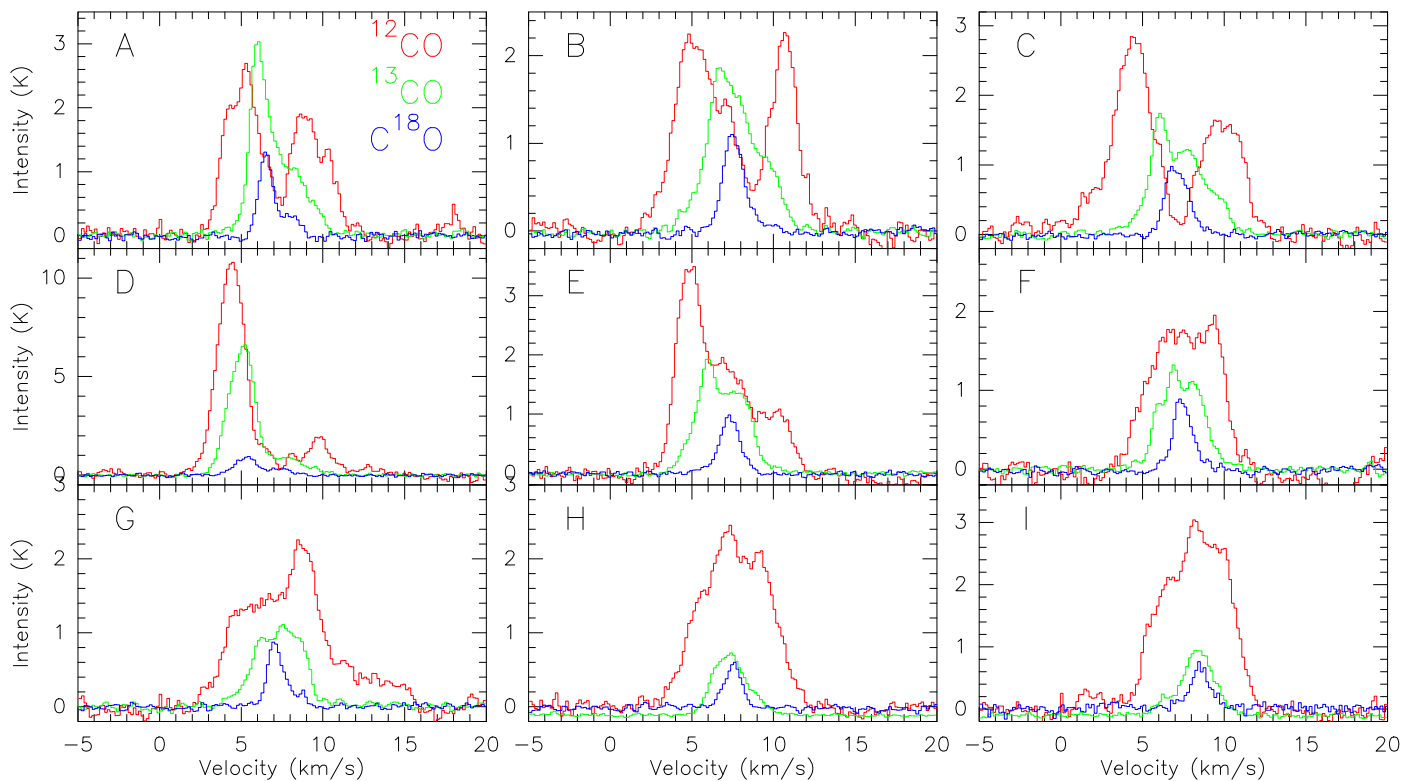


**Fig. 6.** The averaged spectra of  $^{12}\text{CO}(1-0)$  (red),  $^{13}\text{CO}(1-0)$  (green) and  $\text{C}^{18}\text{O}(1-0)$  (blue) emissions at the selected regions from Figure 5. The name of the selected regions presented in the top-left corner in each panel.

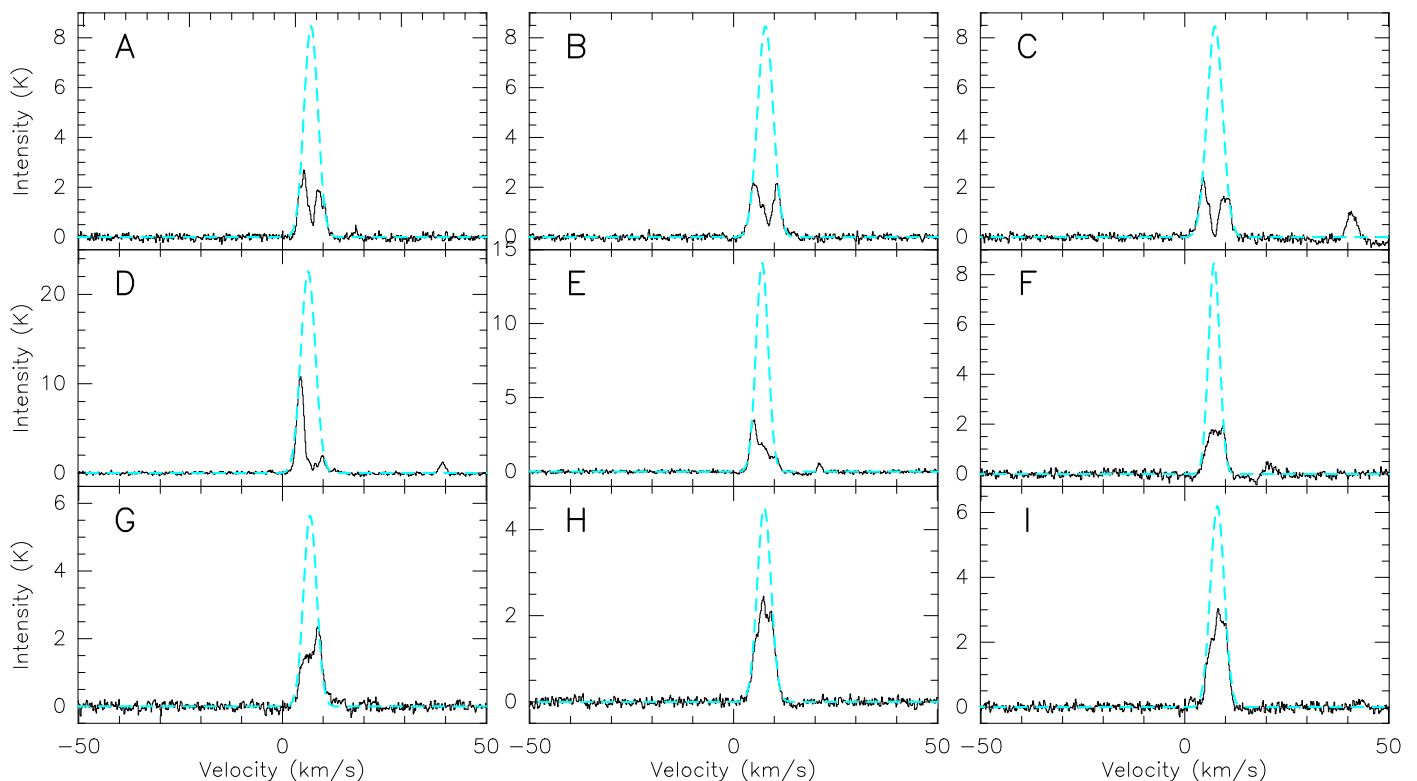


**Fig. 7.** Examples of the  $^{12}\text{CO}$  self-absorption correction. The blue dashed line presents the best single Gaussian fitting for the original  $^{12}\text{CO}$  profile using the remaining wings of the emission line. The name of the selected regions are presented in the top-left corner in each panel.

where  $X_{\text{CO}} = 2 \times 10^{20} (\text{K km s}^{-1})^{-1}$  (Strong et al. 1988).

The average fluxes of the infrared  $70 \mu\text{m}$  and  $250 \mu\text{m}$  images of the distinct regions (see Table 1) were obtained from The

Herschel Gould Belt Survey Archive. The average  $70 \mu\text{m}$  flux is higher in the regions A, B, C, D, E, F, and G, with the highest flux  $\sim 2172 \text{ MJy/sr}$  in the region D next to the W40 HII region.

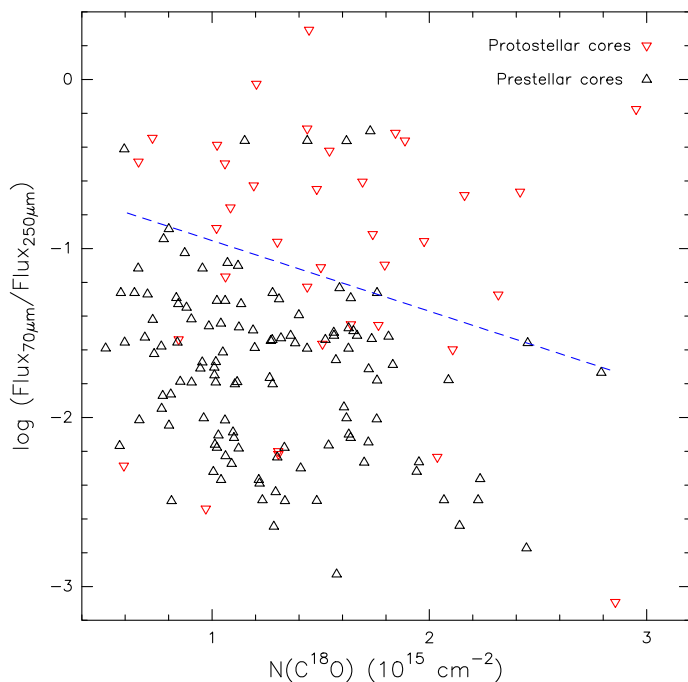


**Fig. 8.** The column density of  $C^{18}O$  vs. the peak flux density ratio of the bandwidth of  $70 \mu\text{m}$  and  $250 \mu\text{m}$  of the protostellar (red triangles) and prestellar (black triangles) cores selected from Könyves et al. (2015). The dotted line indicates the dividing line between prestellar and protostellar cores and shows the gradual change of the ratio.

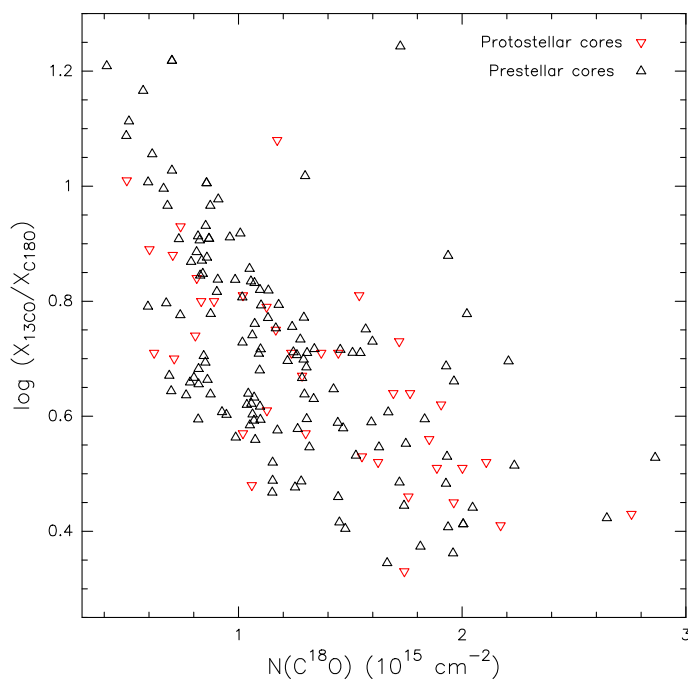


**Fig. 9.** The column density of  $C^{18}O$  versus the abundance ratio  $X_{13CO}/X_{C^{18}O}$  at the protostellar (red triangles) and prestellar (black triangles) cores.

However, it is significantly lower in other regions. It means that the previewed regions are enhanced, and the star-forming processes are going more actively than the last ones.

The results are summarized in Table 1. The columns have the following meaning: Column 1: The distinct region, Column 2

and 3: The right ascension and declination (J2000) of the centre position, Column 4: The radius of the region, Column 5: The average flux of Herschel  $70 \mu\text{m}$  image, Column 6: The average flux of Herschel  $250 \mu\text{m}$  image, Column 7: The original mass based on the best Gaussian fitting, and Column 8: The original luminosity of the  $^{12}CO$  based on the best Gaussian fitting.

### 3.8. Correlating the Infrared and photo-dissociation data

The heating of the interstellar dust by the star formation processes first results in  $250 \mu\text{m}$  infrared emission and at a later stage produce  $70 \mu\text{m}$  emission (eg. Bendo et al. 2015). Therefore, the  $70/250 \mu\text{m}$  ratio could be an indicator of the evolutionary age of the star formation process and the state of the interstellar dust. On the other hand, photo-dissociation is clearly a time-dependent effect resulting from the UV exposure of the molecular gas and the photo-dissociation rate also reflects on the evolutionary age of the selected distinct regions.

The peak flux density at the prestellar and protostellar cores at wavelength of  $70 \mu\text{m}$  vs. the column density of  $C^{18}O(1-0)$  shows a separation between the prestellar and protostellar core distributions (Figure 4a). The variation of the  $250 \mu\text{m}$  emission data suggests a flux density increase at higher  $C^{18}O$  column densities, such that the more intense star formation is able to heat a larger volume of the surrounding dust, which would also be is also time dependent (Figure 4b). Figure 8 displays the column density of  $C^{18}O$  vs. the peak flux density ratio  $F_{70\mu\text{m}}/F_{250\mu\text{m}}$  of protostellar and prestellar cores. Excluding some improperly distributed stellar cores, most evolved protostellar cores are in the upper part, and the youthful prestellar cores are in the lower part in the diagram. However, the dividing line between the flux ratio decreases with an increasing  $C^{18}O$  column density because at higher  $C^{18}O$  columns the star formation have time and energy to heat larger volumes of dust. The flux ratio  $F_{70\mu\text{m}}/F_{250\mu\text{m}}$  diagram confirms that the  $C^{18}O$  column density connects with the evolutionary age of the cores.

The abundance ratio of  $X_{13CO}/X_{C^{18}O}$  for the prestellar and protostellar locations plotted against the  $C^{18}O$  column density shows similar a distribution for prestellar and protostellar cores, which indicates that the effects of photodissociation only depends on the presence of star formation at this  $C^{18}O$  column density (Figure 9). The  $X_{13CO}/X_{C^{18}O}$  abundance ratio decreases with increasing of the  $C^{18}O$  column density indicating the enhancement of  $C^{18}O$  in the ISM. The strong variation of the abundance ratio with the  $C^{18}O$  column density shows that the more massive and fragmented star formation has a strong effect on the surrounding area.

The actual mass of the star formation region containing young stellar objects plays a critical role in distinguishing between evolutionary paths and their timescales. In order to depict the evolutionary path of star formation regions in the Aquila MC, the original mass estimated from the reconstructed  $^{13}CO$  emission line in the nine selected regions has plotted against the  $70 \mu\text{m}$  flux density in Figure 10a. This diagram shows that the regions lie along a string of points indicating five stages of evolution. Region D, next to the W40 HII, belongs to the oldest evolutionary stage with the largest amount of mass ( $\sim 74 M_{\odot}$ ) being photo-dissociated and having the highest  $70 \mu\text{m}$  flux density. The regions B and E form a next oldest stage of evolution, where region B is the Serpens South region and region E is a filament located southeast of the W40 HII. Region E has lost more mass to photo-dissociation than region B. The regions G, F, A, and C are as regions of an earlier stage of evolution, where re-

**Table 1.** The integrated properties of the distinct regions

Reg.	RA	DEC	Area	$F_{70\mu\text{m}}$	$F_{250\mu\text{m}}$	$M_{\text{H}_2}$	$L_{^{12}\text{CO}}$
(1)	J2000	J2000	$\text{pc}^2$	MJy/sr	MJy/sr	$M_{\odot}$	$\text{K kms}^{-1}\text{pc}^2$
(2)	(3)	(4)	(5)	(6)	(7)	(8)	(8)
A	18:29:07.40	-02:05:28	0.97	80.97	416.56	33.48	10.46
B	18:29:57.80	-02:00:04	1.16	187.07	599.29	47.94	14.98
C	18:29:58.78	-02:10:37	1.09	77.51	375.55	41.09	12.84
D	18:31:03.24	-02:05:28	1.09	2171.54	1,319.11	97.17	30.36
E	18:31:57.15	-02:00:14	1.16	236.48	830.95	62.15	19.42
F	18:32:20.73	-02:26:07	0.91	76.29	249.23	26.79	8.37
G	18:31:09.80	-02:25:22	0.97	77.14	268.46	25.98	8.12
H	18:29:21.57	-01:25:00	0.97	8.27	75.84	14.61	4.57
I	18:32:33.50	-01:24:41	0.59	1.00	62.50	6.04	1.89

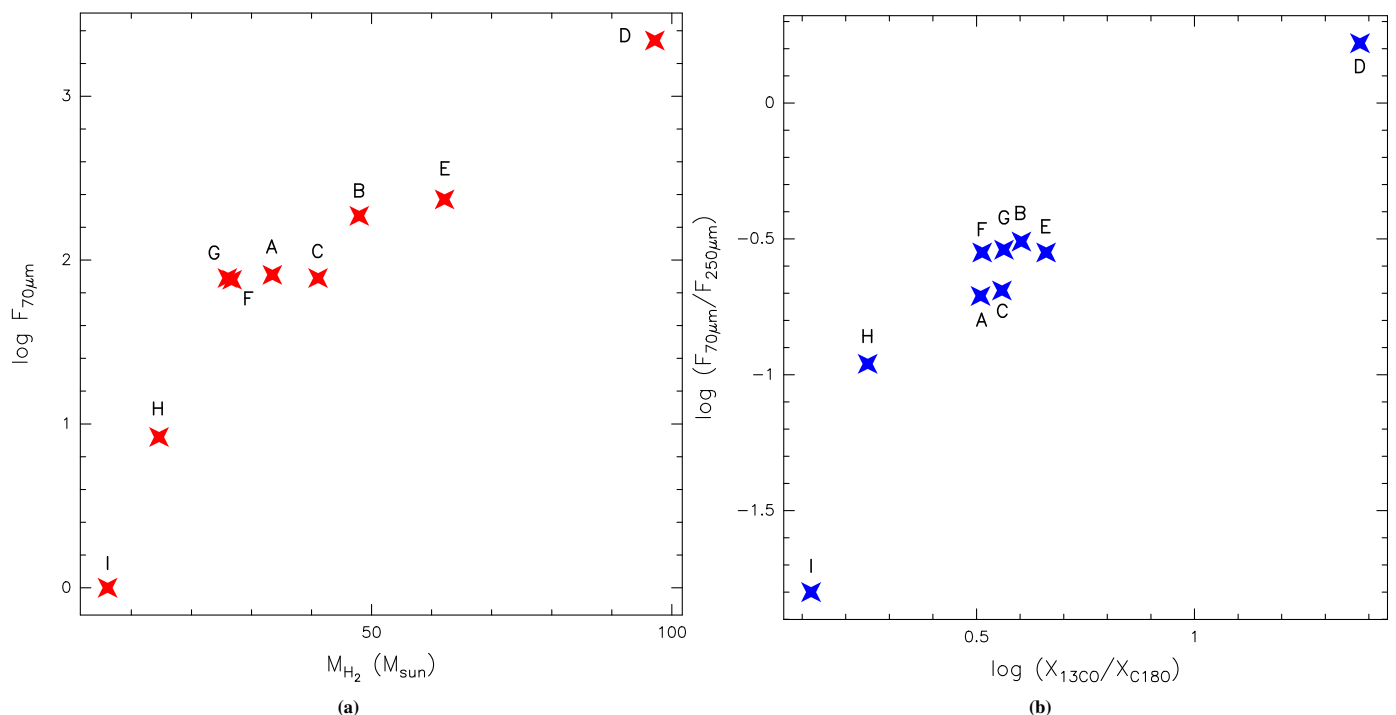


**Fig. 10.** (a) The mass corrected the self-absorption vs. the  $70\ \mu\text{m}$  flux and (b) the ratio  $X_{^{13}\text{CO}}/X_{\text{C}^{18}\text{O}}$ , equivalent to the dissociation rate of the  $\text{C}^{18}\text{O}$ , vs. the flux ratio  $F_{70\mu\text{m}}/F_{250\mu\text{m}}$  of the distinct regions. The letters (A-I) present the selected regions. The average fluxes of infrared  $70\ \mu\text{m}$  and  $250\ \mu\text{m}$  images of the distinct regions in both panels were obtained from the data of The Herschel Gould Belt Survey Archive.

gion C has lost a little more mass than others because it is larger. The youngest star formation region H is just starting to show up in  $70\ \mu\text{m}$  images. Region I is the youngest region located on the outskirts of the cloud; it does not yet show any  $70\ \mu\text{m}$  flux and it has the smallest estimated mass of all regions.

Since UV radiation selectively dissociates less-abundant CO isotopologues more effectively than more-abundant ones (van Dishoeck & Black 1988; Liszt 2007; Shimajiri et al. 2014) the ratio  $X_{^{13}\text{CO}}/X_{\text{C}^{18}\text{O}}$  is equivalent to the dissociation rate of the  $\text{C}^{18}\text{O}$ . Similar evolutionary sequence is found when plotting the ratio  $X_{^{13}\text{CO}}/X_{\text{C}^{18}\text{O}}$  versus the flux ratio  $F_{70\mu\text{m}}/F_{250\mu\text{m}}$  of the selected regions in Figure 10b. However, the mid-range evolutionary regions cluster together in this case, possibly due to inaccuracies in estimating the abundance ratio. The two diagrams of Figure 10 presents the original mass and the rate of photodissociation combined with the infrared properties are useful to determine the evolutionary age of the star-forming regions.

### 3.9. Uncertainties of the abundance ratio $X_{^{13}\text{CO}}/X_{\text{C}^{18}\text{O}}$ introduced by the excitation temperature and the beam-filling factor

$\text{C}^{18}\text{O}$  and  $^{13}\text{CO}$  beam-filling factors were assumed to be unity when estimating their column densities and optical depths in Sect. 3.4. Also, the excitation temperatures ( $T_{\text{ex}}$ ) for all the three lines  $\text{C}^{18}\text{O}$ ,  $^{13}\text{CO}$  and  $^{12}\text{CO}$  were presumed to be the same values which were derived from the optically thick line  $^{12}\text{CO}$ .

Calculation of the beam-filling factor is obtained through equation (8).

$$f = \frac{\theta_s^2}{\theta_s^2 + \theta_{\text{beam}}^2} \quad (8)$$

where  $\theta_{\text{beam}}$  is the beam size and  $\theta_s$  is source diameter. The  $^{13}\text{CO}$  and  $\text{C}^{18}\text{O}$  data have an effective beam size of  $60''$  corresponding to  $0.124\ \text{pc}$  at the distance of the Aquila MC.  $\text{C}^{18}\text{O}$  emission is deemed as a tracer of dense cores, filaments, and clumps. In comparison, the  $^{13}\text{CO}$  emission will additionally trace extended

**Table 2.** Column densities and abundance ratio  $X_{^{13}\text{CO}}/X_{\text{C}^{18}\text{O}}$  of  $^{13}\text{CO}$  and  $\text{C}^{18}\text{O}$ 

Molecule	$T_{\text{ex}}$	Beam-filling factor	Column density	$X_{^{13}\text{CO}}/X_{\text{C}^{18}\text{O}}$
$^{13}\text{CO}$	$T_{\text{ex}}(^{12}\text{CO})$	1	$0.38\text{--}55.34 \times 10^{15} \text{cm}^{-2}$	1.02–41.9
$\text{C}^{18}\text{O}$	$T_{\text{ex}}(^{12}\text{CO})$	1	$0.21\text{--}3.42 \times 10^{15} \text{cm}^{-2}$	
$^{13}\text{CO}$	$T_{\text{ex}}(^{12}\text{CO})$	0.6	$0.77\text{--}70.41 \times 10^{15} \text{cm}^{-2}$	0.99–40.1
$\text{C}^{18}\text{O}$	$T_{\text{ex}}(^{12}\text{CO})$	0.6	$0.43\text{--}15.11 \times 10^{15} \text{cm}^{-2}$	
$^{13}\text{CO}$	30 K	1	$0.72\text{--}49.61 \times 10^{15} \text{cm}^{-2}$	1.39–32.88
$\text{C}^{18}\text{O}$	20 K	1	$0.28\text{--}4.17 \times 10^{15} \text{cm}^{-2}$	
$^{13}\text{CO}$	30 K	0.6	$0.14\text{--}16.4 \times 10^{16} \text{cm}^{-2}$	1.38–32.88
$\text{C}^{18}\text{O}$	20 K	0.6	$0.57\text{--}9.21 \times 10^{15} \text{cm}^{-2}$	

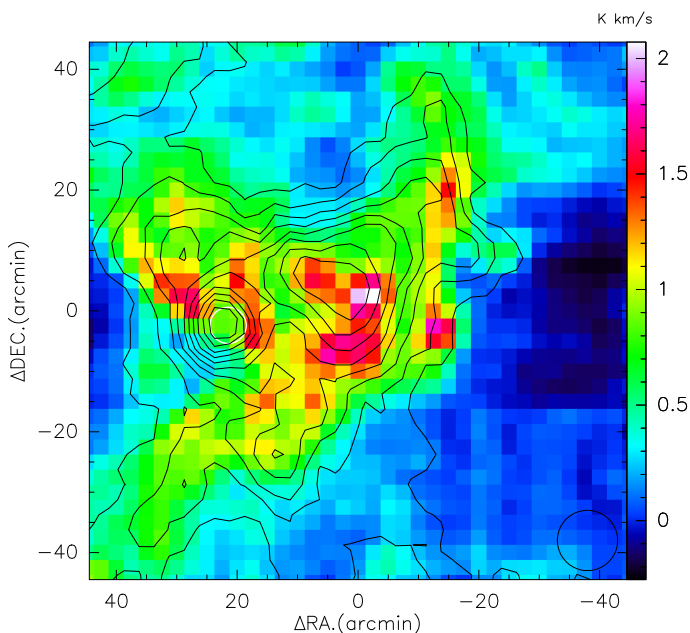


**Fig. 11.** A map of the  $\text{C}^{18}\text{O}(1-0)$  integrated intensity superposed on the contours of  $\text{H}_2\text{CO}$  absorption toward the Aquila molecular cloud. The  $\text{C}^{18}\text{O}(1-0)$  and  $\text{H}_2\text{CO}$  data have been smoothed to the same effective resolution and cell size of  $10'$  and  $2.5'$ , respectively. Contour levels of the  $\text{H}_2\text{CO}$  intensity map are  $-0.4$  to  $-1.8$  in steps of  $-0.15 \text{K km s}^{-1}$ . The white circle present the location of the W40 HII region (radius  $\sim 3'$ ) and the black circle in the bottom-right illustrates the resolution of  $10'$ .

components which could be seen via integrated intensity maps (Shimajiri et al. 2014). The nearest low-mass star forming region observations toward the Taurus cloud traced via  $\text{C}^{18}\text{O}$  have dense cores of  $0.1 \text{pc}$  diameter (Onishi et al. 1996). Moreover, the constant encounter of parsec-scale filaments with narrow widths of typically  $0.1 \text{pc}$  within molecular clouds are discovered through Herschel micrometre emission observations (Arzoumanian et al. 2011; Palmeirim et al. 2013). This infers that traced  $^{13}\text{CO}$  and  $\text{C}^{18}\text{O}$  sources will have dimensions over  $0.1 \text{pc}$ . Assuming  $\theta_{\text{source}} > 0.1 \text{pc}$  and  $\theta_{\text{beam}} = 0.124 \text{pc}$ , we anticipate the beam to exceed  $0.6$ . The affect of the beam filling factor towards the abundance ratios and column densities are summarized in Tabel 2. The column density values both of  $\text{C}^{18}\text{O}$  and  $^{13}\text{CO}$  with the assumption of  $\phi=0.6$  increase compared with those of  $\phi=1$ . Nevertheless, the beam filling factor corrections play a insignificant role on estimating  $X_{^{13}\text{CO}}/X_{\text{C}^{18}\text{O}}$

Since  $^{12}\text{CO}$  emission is affected by the self-absorption,  $\text{C}^{18}\text{O}$  and  $^{13}\text{CO}$  column densities are affected by underestimates of  $T_{\text{ex}}$  from the  $^{12}\text{CO}$  data. The influence of un-

certainties in excitation temperature towards derived physical properties is investigated assuming  $T_{\text{ex}}(\text{C}^{18}\text{O})=20 \text{K}$  and  $T_{\text{ex}}(^{13}\text{CO})=30 \text{K}$ . This is further illustrated in Table 2. The column density values both of  $^{13}\text{CO}$  and  $\text{C}^{18}\text{O}$  with the assumption of  $T_{\text{ex}}(\text{C}^{18}\text{O})=20 \text{K}$  and  $T_{\text{ex}}(^{13}\text{CO})=30 \text{K}$  increase compared with those of  $T_{\text{ex}}(^{13}\text{CO})=T_{\text{ex}}(\text{C}^{18}\text{O})=T_{\text{ex}}(^{12}\text{CO})$ . However, the range of the  $X_{^{13}\text{CO}}/X_{\text{C}^{18}\text{O}}$  with  $T_{\text{ex}}(\text{C}^{18}\text{O})=20 \text{K}$  and  $T_{\text{ex}}(^{13}\text{CO})=30 \text{K}$  are slightly narrower compared with those of  $T_{\text{ex}}(^{13}\text{CO})=T_{\text{ex}}(\text{C}^{18}\text{O})=T_{\text{ex}}(^{12}\text{CO})$ . The higher abundance ratios ( $X_{^{13}\text{CO}}/X_{\text{C}^{18}\text{O}} > 10$ ) in all assumptions correspond to the region D, next to the W40 HII.

In supposition following the inclusion of the uncertainties of excitation temperatures and beam filling factors of  $^{13}\text{CO}$  and  $\text{C}^{18}\text{O}$  we are convinced, with one exception of resulting high abundance ratio region (next to the W40 HII), the abundance ratio  $X_{^{13}\text{CO}}/X_{\text{C}^{18}\text{O}}$  is lower toward the other star-forming hot spots in the Aquila MC.

### 3.10. A comparison with $\text{H}_2\text{CO}$ absorption

Since regions B, D, and G have been identified as distinct star formation regions in the  $\text{H}_2\text{CO}$  absorption map of the Aquila MC, a comparison may be made between the  $\text{C}^{18}\text{O}$  distribution and the  $\text{H}_2\text{CO}$  absorption (Komesh et al. 2019). Figure 11 shows a map of the  $\text{C}^{18}\text{O}(1-0)$  integrated intensity superposed on the integrated absorption contours of  $\text{H}_2\text{CO}$ . The  $\text{C}^{18}\text{O}(1-0)$  and  $\text{H}_2\text{CO}$  data have been smoothed to the same effective resolution and cell size of  $10'$  and  $2.5'$ , respectively. The outer edges of the  $\text{C}^{18}\text{O}$  emission ( $\sim 0.7 \text{K km s}^{-1}$ ) follow the lower contours of  $\text{H}_2\text{CO}$  ( $\sim 0.4 \text{K km s}^{-1}$ ) and the contours encompass all identified star formation regions in the  $\text{C}^{18}\text{O}$  data. The stronger  $\text{C}^{18}\text{O}$  emission surrounding W40 does not correspond to the  $\text{H}_2\text{CO}$  absorption, because the  $\text{H}_2\text{CO}$  absorption is related to the radio continuum of the HII region while the enhanced  $\text{C}^{18}\text{O}$  emission results from heating by the HII region. The  $\text{C}^{18}\text{O}$  emission map at Serpens South shows several elongated structures that only partially follow the  $\text{H}_2\text{CO}$  absorption structure. On a large scale the  $\text{H}_2\text{CO}$  absorption structure is similar to the  $\text{C}^{18}\text{O}(1-0)$  distribution but it does not identify all active star formation regions.

## 4. Conclusion

Archival data of wide-field OTF observations of  $^{12}\text{CO}$ ,  $^{13}\text{CO}$ , and  $\text{C}^{18}\text{O}$  ( $J=1-0$ ) emission lines of the Aquila molecular cloud have been used to study the star formation activity in the region and the influence on the surroundings. In Aquila MC the distribution of protostellar and prestellar cores are a first indication of the locations of active star formation and their distribution is well correlated with the highest column densities within the structure of the extended  $\text{C}^{18}\text{O}(1-0)$  emission. This extended

star formation structure is also found within the contours of the  $\text{H}_2\text{CO}$  absorption against the continuum of the region.

The abundance ratio  $X_{^{13}\text{CO}}/X_{\text{C}^{18}\text{O}}$  in our observations confirm that selective FUV photodissociation of  $\text{C}^{18}\text{O}$  indeed occurs. Since photo-dissociation results from FUV exposure of the surrounding molecular gas, photo-dissociation is a time dependent process that may serve as an indicator of the evolutionary age of the star formation. This effect is confirmed by a strong reduction of the abundance ratio  $X_{^{13}\text{CO}}/X_{\text{C}^{18}\text{O}}$  versus the  $\text{C}^{18}\text{O}$  column density.

To evaluate how the beam filling factor affects  $X_{^{13}\text{CO}}/X_{\text{C}^{18}\text{O}}$  abundance ratio, we estimated the beam filling factor to exceed 0.6 for both  $\text{C}^{18}\text{O}$  and  $^{13}\text{CO}$  gas. The abundance ratio  $X_{^{13}\text{CO}}/X_{\text{C}^{18}\text{O}}$  distribution in the Aquila MC were found to be similar even after the consideration of uncertainties of the beam filling factor. The beam filling factor corrections play a insignificant role on estimating  $X_{^{13}\text{CO}}/X_{\text{C}^{18}\text{O}}$

Since the  $^{12}\text{CO}$  emission affected by the self-absorption  $\text{C}^{18}\text{O}$  and  $^{13}\text{CO}$  column densities are effected by underestimates of  $T_{\text{ex}}$  (3.6–23.6 K) from the  $^{12}\text{CO}$  data. To study the affects of the uncertainties in excitation temperature towards acquired physical properties, we use the assumption of  $T_{\text{ex}}(\text{C}^{18}\text{O})=20$  K and  $T_{\text{ex}}(^{13}\text{CO})=30$  K. Even if we consider higher excitation temperatures for the  $^{13}\text{CO}$  and  $\text{C}^{18}\text{O}$  line, we come to the same conclusion that, with exception of one high abundance ratio region (next to the W40 HII), the abundance ratio  $X_{^{13}\text{CO}}/X_{\text{C}^{18}\text{O}}$  is lower toward the other starforming hot spots in the Aquila MC.

The FUV radiation field originating at the location of massive and even fragmented star formation will also heat the surround molecular regions. This heating process will increasingly result in  $250 \mu\text{m}$  FIR emission and after a certain evolutionary period also  $70 \mu\text{m}$  emission. The  $70/250 \mu\text{m}$  flux density ratio could then also serve as an evolutionary age indicator and this ratio is indeed found to vary with the  $\text{C}^{18}\text{O}$  column density.

These evolutionary indicators have been tested with a number of selected star-formation and non-star-formation regions for which the dissociation rate have been estimated by the ratio  $X_{^{13}\text{CO}}/X_{\text{C}^{18}\text{O}}$ . A clear sequence for these selected regions has been found when correlating the  $70 \mu\text{m}$  flux density with the estimated original mass of the regions. Similarly a clear sequence has been found when correlating the  $70/250 \mu\text{m}$  flux density ratio with the estimated photo-dissociation rate. These observed parameters of the molecular medium surrounding the star formation provide a measure of the intensity of the star formation process as well as a measure of the evolutionary age of the region.

*Acknowledgements.* This work was sponsored by CAS-TWAS President's Fellowship for International Doctoral Students, and The National Natural Science foundation of China under grants 11433008, 11973076, 11703074, 11703073 and 11603063. WAB has been funded by Chinese Academy of Sciences President's International Fellowship Initiative under grants 2021VMA0008 and 2019VMA0040. Collaboration between ZR and the main author was supported by the University of Malaya grant UMRG FG033-017AFR. This publication makes use of data products from the 13.7m telescope of the Qinghai observation station of the Purple Mountain Observatory and the millimeter wave radio astronomy database, and the data from the Herschel Gould Belt survey (HGBS) project (<http://gouldbelt-herschel.cea.fr>). The HGBS is a Herschel Key Programme jointly carried out by SPIRE Specialist Astronomy Group 3 (SAG 3), scientists of several institutes in the PACS Consortium (CEA Saclay, INAF-IFSI Rome and INAF-Arcetri, KU Leuven, MPIA Heidelberg), and scientists of the Herschel Science Center (HSC).

André, P., Men'shchikov, A., Bontemps, S., et al. 2010, A&A, 518, L102  
 Arzoumanian, D., André, P., Didelon, P., et al. 2011, A&A, 529, L6  
 Bendo, G. J., Baes, M., Bianchi, S., et al. 2015, MNRAS, 448, 135  
 Bontemps, S., André, P., Könyves, V., et al. 2010, A&A, 518, L85  
 Glassgold, A. E., Huggins, P. J., & Langer, W. D. 1985, ApJ, 290, 615  
 Gutermuth, R. A., Bourke, T. L., Allen, L. E., et al. 2008, ApJ, 673, L151  
 Kawamura, A., Onishi, T., Yonekura, Y., et al. 1998, ApJS, 117, 387  
 Kim, S.-J., Kim, H.-D., Lee, Y., et al. 2006, ApJS, 162, 161  
 Komesch, T., Esimbek, J., Baan, W., et al. 2019, ApJ, 874, 172  
 Kong, S., Lada, C. J., Lada, E. A., et al. 2015, ApJ, 805, 58  
 Könyves, V., André, P., Men'shchikov, A., et al. 2015, A&A, 584, A91  
 Lada, C. J., Lada, E. A., Clemens, D. P., et al. 1994, ApJ, 429, 694  
 Liszt, H. S. 2007, A&A, 476, 291  
 Lin, S.-J., Shimajiri, Y., Hara, C., et al. 2016, ApJ, 826, 193  
 Onishi, T., Mizuno, A., Kawamura, A., et al. 1996, ApJ, 465, 815  
 Ortiz-León, G. N., Dzib, S. A., Kounkel, M. A., et al. 2017, ApJ, 834, 143  
 Palmeirim, P., André, P., Kirk, J., et al. 2013, A&A, 550, A38  
 Pineda, J. L., Goldsmith, P. F., Chapman, N., et al. 2010, ApJ, 721, 686  
 Shimajiri, Y., Kitamura, Y., Saito, M., et al. 2014, A&A, 564, A68  
 Smith, J., Bentley, A., Castelaz, M., et al. 1985, ApJ, 291, 571  
 Strong, A. W., Bloemen, J. B. G. M., Dame, T. M., et al. 1988, A&A, 207, 1  
 Su, Y., Yang, J., Yan, Q.-Z., et al. 2020, ApJ, 893, 91  
 Tan, B.-K., Leech, J., Rigopoulou, D., et al. 2013, MNRAS, 436, 921  
 Tielens, A. G. G. M., & Hollenbach, D. 1985, ApJ, 291, 722  
 Ulich, B. L., & Haas, R. W. 1976, ApJS, 30, 247  
 van Dishoeck, E. F., & Black, J. H. 1988, ApJ, 334, 771  
 Yurimoto, H., & Kuramoto, K. 2004, Science, 305, 1763

## References

Anders, E., & Grevesse, N. 1989, Geochim. Cosmochim. Acta, 53, 197